

Melt Growth and Physical Properties of Bulk LaInO_3 Single Crystals


Zbigniew Galazka,* Klaus Irmscher, Steffen Ganschow, Martina Zupancic, Wahib Aggoune, Claudia Draxl, Martin Albrecht, Detlef Klimm, Albert Kwasniewski, Tobias Schulz, Mike Pietsch, Andrea Dittmar, Raimund Grueneberg, Uta Juda, Robert Schewski, Sabine Bergmann, Hyeongmin Cho, Kookrin Char, Thomas Schroeder, and Matthias Bickermann

Large bulk LaInO_3 single crystals are grown from the melt contained within iridium crucibles by the vertical gradient freeze (VGF) method. The obtained crystals are undoped or intentionally doped with Ba or Ce, and enabled wafer fabrication of size $10 \times 10 \text{ mm}^2$. High melting point of LaInO_3 ($\approx 1880^\circ\text{C}$) and thermal instability at high temperatures require specific conditions for bulk crystal growth. The crystals do not undergo any phase transition up to 1300°C , above which a noticeable thermal decomposition takes place. The good structural quality of the crystals makes them suitable for epitaxy. The onset of strong optical absorption shows orientation-dependent behavior due to the orthorhombic symmetry of the LaInO_3 crystals. Assuming direct transitions, optical bandgaps of 4.35 and 4.39 eV are obtained for polarizations along the [010] and the [100], [001] crystallographic directions, respectively. There is an additional weak absorption in the range between 2.8 and 4 eV due to oxygen vacancies. Density-functional-theory calculations support the interpretation of the optical absorption data. Cathodoluminescence spectra show a broad, structured emission band peaking at ≈ 2.2 eV. All bulk crystals are electrically insulating. The relative static dielectric constant is determined at a value of 24.6 along the [001] direction.

1. Introduction

LaInO_3 has been indicated in the literature as a potential material for solid oxide fuel cells (SOFCs)^[1–3] due to high oxide ionic conductivity when doped with Sr and also as phosphor^[4] when doped with rare-earth ions. Recent advances in growing high-mobility BaSnO_3 opened another application for LaInO_3 , that is, a heterostructure of the nonpolar BaSnO_3 —a polar LaInO_3 system to generate a 2D electron gas (2DEG). Indeed, BaSnO_3 -based field-effect transistors comprising a LaInO_3 gate dielectric with the generation of the 2DEG has been successfully demonstrated.^[5–8] LaInO_3 is also a potential candidate as a lattice-matched substrate for epitaxial growth of cubic BaSnO_3 . When considering bulk LaInO_3 single crystals as substrates, a pseudocubic LaInO_3 lattice parameter $a_{\text{pc}} = \frac{1}{2}\sqrt{a^2 + c^2} = 4.123 \text{ \AA}$ of the orthorhombic structure matches the cubic lattice parameter of BaSnO_3 , which is $a = 4.117 \text{ \AA}$.^[9] This favor-

Dr. Z. Galazka, Dr. K. Irmscher, Dr. S. Ganschow, M. Zupancic, Dr. M. Albrecht, Dr. D. Klimm, A. Kwasniewski, Dr. T. Schulz, M. Pietsch, Dr. A. Dittmar, R. Grueneberg, Dr. U. Juda, Dr. R. Schewski, S. Bergmann, Prof. T. Schroeder, Prof. M. Bickermann
Department of Volume Crystals
Leibniz-Institut für Kristallzüchtung
Max-Born-Str. 2, 12489 Berlin, Germany
E-mail: zbigniew.galazka@ikz-berlin.de

 The ORCID identification number(s) for the author(s) of this article can be found under <https://doi.org/10.1002/pssa.202100016>.

© 2021 The Authors. *physica status solidi (a)* applications and materials science published by Wiley-VCH GmbH. This is an open access article under the terms of the Creative Commons Attribution-NonCommercial-NoDerivs License, which permits use and distribution in any medium, provided the original work is properly cited, the use is non-commercial and no modifications or adaptations are made.

DOI: 10.1002/pssa.202100016

Dr. W. Aggoune, Prof. C. Draxl
Institut für Physik and IRIS Adlershof
Humboldt-Universität zu Berlin
Zum Großen Windkanal 2, 12489 Berlin,
Germany

H. Cho, Prof. K. Char
Institute of Applied Physics
Department of Physics and Astronomy
Seoul National University
Seoul 08826, South Korea

Prof. T. Schroeder
Institut für Physik
Humboldt-Universität zu Berlin
Newtonstr. 15, 12489 Berlin, Germany

Prof. M. Bickermann
Institut für Chemie
Technische Universität Berlin
Straße des 17. Juni 115, 10623 Berlin, Germany

able epitaxial relation could stimulate demand for LaInO₃ substrates as a substitute for native BaSnO₃ substrates as the growth of bulk BaSnO₃ crystals of a reasonable size is really challenging.^[10–15]

The literature demonstrates the preparation of ceramic samples by solid-state synthesis^[1–3] and film growth of LaInO₃,^[5,16,17] along with some of the physical properties, but to the best of our knowledge, there are only two available reports on bulk single crystals obtained by the optical floating zone (OFZ) method.^[12,18] The OFZ-grown crystal was about 6 mm in diameter and exhibited a dark brown color. From this crystal, a polished wafer of about 3 × 4 × 0.3 mm³ could be prepared that was transparent. However, the measured full width at half maximum (FWHM) of the rocking curve of at best 120 arcsec indicates that the crystals still contain structural defects, like grain boundaries. The availability of the crystal samples enabled determination of some of the optical properties, in particular, the optical bandgap.

In the present work, we describe the capability of growing large LaInO₃ single crystals from the melt contained within an iridium crucible. The obtained crystals are of high structural quality and enable to fabricate epi-ready wafers of a size up to 10 × 10 mm², as well as to accurately explore intrinsic physical properties of LaInO₃, which may serve as a reference for the investigation of differently synthesized LaInO₃ samples (layers, ceramics, powders, nanocrystals). Furthermore, using bulk LaInO₃ single crystals of high structural quality as substrates for epitaxial growth of BaSnO₃ may significantly improve the performance of devices based on these heterostructures, such as high-electron-mobility transistors.

2. Results and Discussion

2.1. Crystal Growth

In the ternary La–In–O system, La₂O₃ is thermally stable at high temperatures, but In₂O₃ undergoes a substantial decomposition with In₂O and O₂ as the most volatile species.^[19,20] As a result, this ternary system will experience incongruent decomposition and evaporation, leading to a fast shift of the chemical composition, as similarly observed for BaSnO₃^[15] or ZnGa₂O₄.^[21] We measured by a two-color pyrometer the melting point (MP) of LaInO₃ directly on the melt surface and obtained a value of MP = 1880 °C ± 15 K. This temperature is high enough for significant losses of In-containing species In₂O(g) and In(g), as shown in **Figure 1**, along with the most volatile La-containing species, LaO(g), where (g) stands for the gas phase. At MP, the ratio of partial pressures of In₂O to LaO, $p(\text{In}_2\text{O})/p(\text{LaO})$, is at the level of six orders of magnitude. For instance, at MP, $p(\text{In}_2\text{O})/p(\text{LaO}) = 8.7 \times 10^6$ at 10% O₂ and 2.2×10^6 at 100% O₂ in the growth atmosphere. During this decomposition process, however, the species having the highest partial pressure is oxygen, $p(\text{O}_2) = 0.156$ atm. at MP, which is higher than that in the initial growth atmosphere (0.1 atm). This means enhanced oxygen losses from the system La₂O₃–In₂O₃ during growth.

Even pure oxygen in the growth atmosphere will not decrease the incongruent evaporation noticeably. Therefore, for bulk crystal growth of LaInO₃, further measures were implemented, such as incongruent starting composition with In₂O₃ excess, relatively short growth time, short soak time of the liquid phase, and a

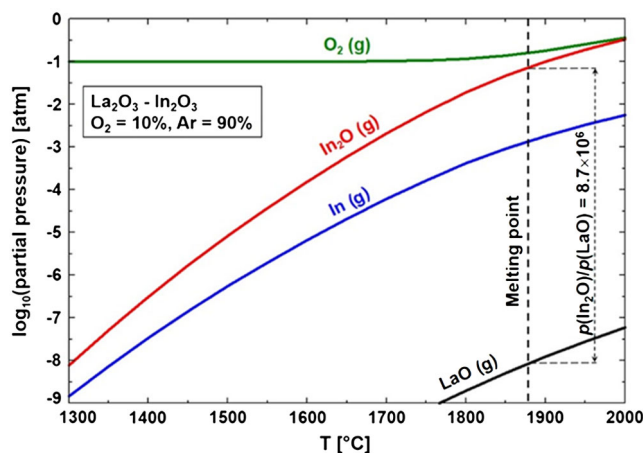


Figure 1. Calculated partial pressures (p) of the most volatile species in the La₂O₃–In₂O₃ system (1 mole each of La₂O₃ and In₂O₃) at O₂ = 0.1 mole + Ar = 0.9 mole.

proper growth method. The starting composition was of a general formula LaIn_(1+x)O₃ with $x = 0–0.1$ (yielding best results with $x = 0.03–0.05$), heating and cooling times of 5–8 h, soak time of the melt below 1 h, O₂ concentration in the growth atmosphere of 9–14 vol.%, whereas growth method was vertical gradient freeze (VGF) using Ir crucibles of 40 mm in diameter and 40–60 mm in height with either a flat or conical bottom. Some of the starting compositions were also doped with BaO or CeO₂. Doping with Ba²⁺ aimed to potentially induce p -type conductivity, as a reverse scheme to doping BaSnO₃ with La³⁺, whereas doping with Ce³⁺ aimed to achieve a new potential scintillator. The advantage of the latter purpose is a high density of LaInO₃ (7.29 g cm^{–3}[22]) and a very good ionic radii match between La³⁺ and Ce³⁺, enabling high Ce³⁺ doping levels. Moreover, high doping levels can be used to modify lattice constants of LaInO₃ wafers dedicated for epitaxy.

Undoped and intentionally Ba-doped LaInO₃ solidified in the Ir crucibles are shown in **Figure 2a,b**, respectively. The solidified material typically consisted of several LaInO₃ single-crystal grains with a volume of 0.5–2.5 cm³ that enabled wafer fabrication with a size up to 10 × 10 mm² (**Figure 2c**) in all main orientations (100), (010), (001), and (110). The extracted single-crystal pieces were free from visual cracks, grains, or inclusions. As-grown undoped and Ce-doped LaInO₃ crystals were yellow, whereas Ba-doped were red. The rough top surface of crystallized LaInO₃ shown in **Figure 2a,b** is the result of In₂O₃ condensation thereon from the gas phase in the following reaction, In₂O(g) + O₂(g) ⇌ In₂O₃(s), where (s) stands for solid.

2.2. Composition and Structural Quality

An X-ray diffraction (XRD) pattern of a powdered, undoped LaInO₃ crystal is shown in **Figure 3**. It has a large number of reflections with a good match to the powder diffraction file (PDF) 01-083-6124.^[23] This suggests the presence of the orthorhombic phase of LaInO₃ within measurement accuracy. In addition, we measured the following lattice parameters on bulk LaInO₃ crystals at room temperature (RT): $a = 5.9380$ Å, $b = 8.2143$ Å, and $c = 5.7227$ Å ± 0.0005(6) Å in the $Pnma$ space

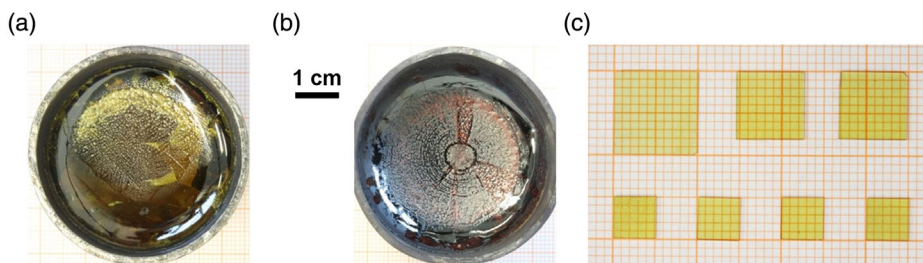


Figure 2. Crystallized LaInO_3 material within Ir crucibles: a) undoped and b) Ba-doped and c) fabricated (110)-oriented wafers from an undoped crystal.

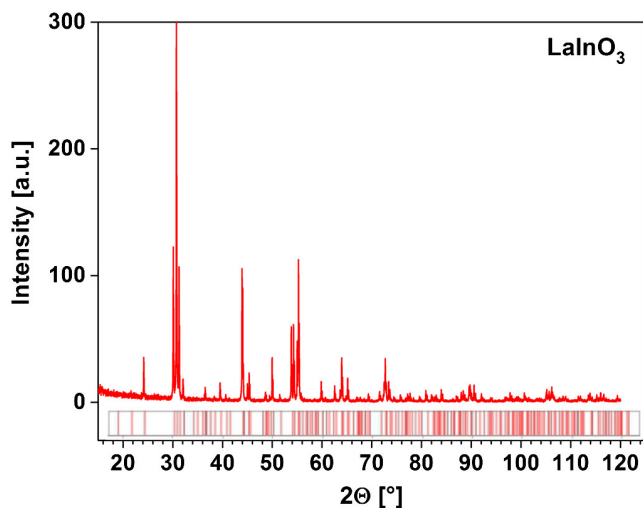


Figure 3. XRD pattern of a powdered bulk LaInO_3 single crystal at RT.

group of the orthorhombic structure, which are comparable with those determined from ceramics^[1,24,25] and bulk crystals.^[18]

The chemical composition of undoped and doped LaInO_3 crystals extracted from different positions within an Ir crucible is shown **Figure 4**. From the measurements it can be concluded that the crystals are very close to stoichiometric composition with a small deficiency of In. Doping with Ba and Ce decreases the La content in the crystals, suggesting that La^{3+} ions are replaced by either Ba^{2+} or Ce^{3+} in the crystal lattice. Considering the ionic radii of La^{3+} (1.36 Å, CN = 12), Ba^{2+} (1.61 Å, CN = 12), and Ce^{3+} (1.34 Å, CN = 12), such substitution is possible for both ions, whereby it should be very effective for Ce^{3+} and less effective for Ba^{2+} . In^{3+} ionic radius (0.8 Å, CN = 6) is too small to be substituted by any of Ba^{2+} or Ce^{3+} .

The structural quality of the obtained bulk LaInO_3 crystals, that is, fabricated wafers, was determined by rocking curve measurements (**Figure 5**), surface roughness determination (**Figure 6**), scanning electron microscopy (SEM) (**Figure 7**), and transmission electron microscopy (TEM) studies (**Figure 8**).

The FWHM values of the rocking curves of fabricated wafers were between 57 and 80 arcsec for the main orientations (100), (010). Such values of FWHMs and sharp peaks with no indication of grains or twins define a good structural quality that is sufficient for epitaxial purposes. It should be noticed, however, that twins occurred in Ba-doped LaInO_3 crystals, likely due to ionic radii mismatch between La^{3+} and Ba^{2+} .

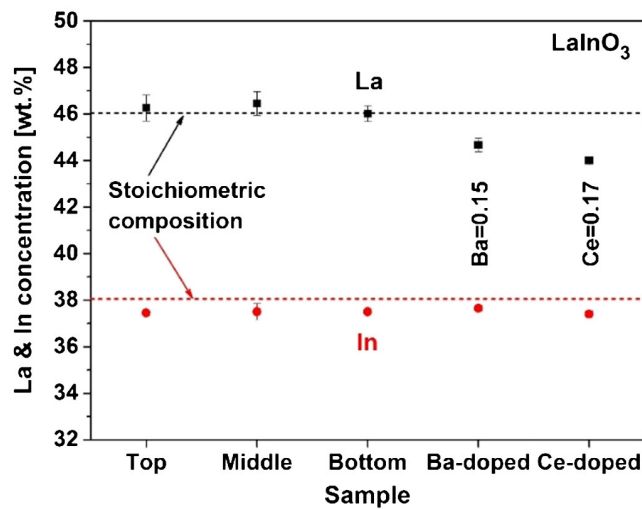


Figure 4. La and In concentrations (in wt%) measured in crystal samples extracted from the top, middle, and bottom parts of the crystallized material within an Ir crucible, as well as crystal samples doped with Ba and Ce, whose concentrations are also given in wt%. Error bars that are not visible on some of the scatters are smaller than the scatter size.

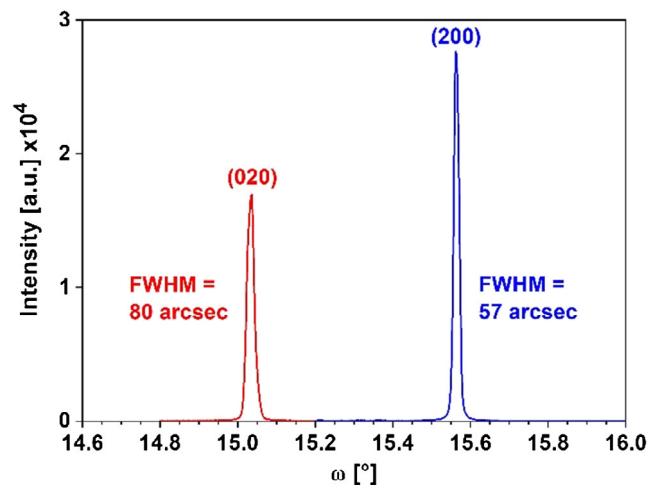


Figure 5. Rocking curve of differently oriented LaInO_3 wafers.

An atomic force microscopy (AFM) evaluation of as-grown and as-polished wafers showed a root mean square (RMS) surface roughness of 0.6, 1.8, and 1.09 nm for (100), (010), and

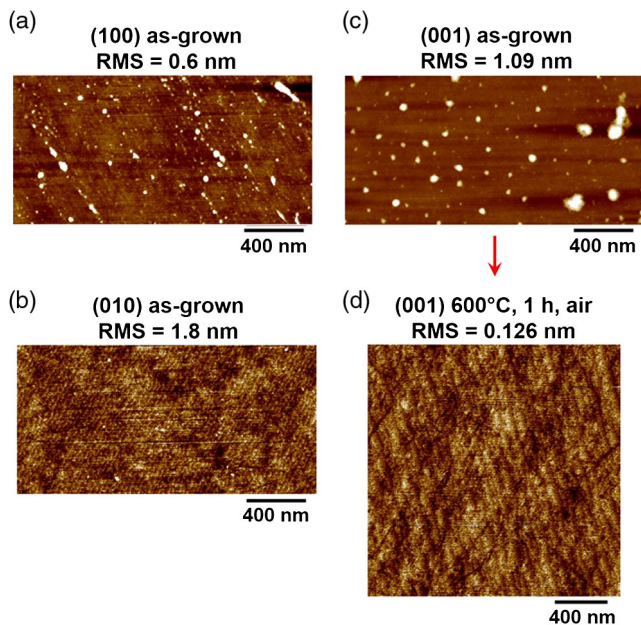


Figure 6. AFM images of LaInO_3 wafers: a–c) as-polished (100), (010), and (010) oriented and d) annealed at 600°C for 1 h in air, (001) oriented.

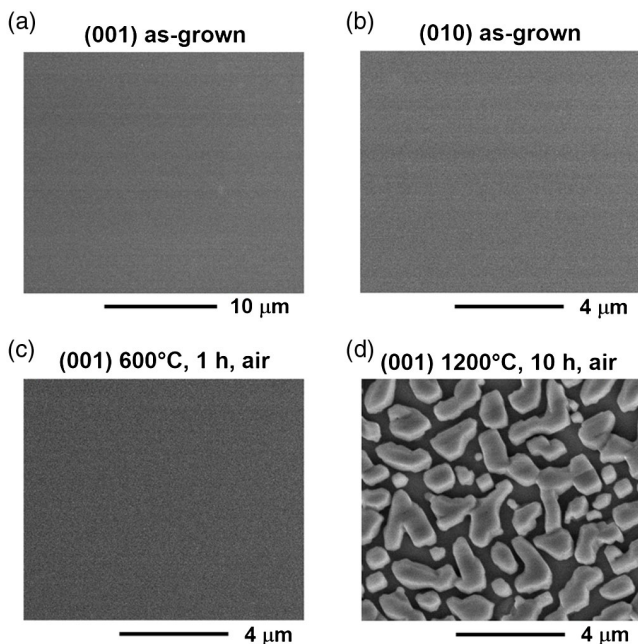


Figure 7. Surface analysis of LaInO_3 wafers by SEM: a,b) as grown with (001) and (010) orientation, c) (001) oriented and annealed at 600°C for 1 h in air; and d) (001) oriented and annealed at 1200°C for 10 h in air.

(001)-oriented wafers with no terraces thereon (Figure 6a–c). White spots visible on the (100) and (001) surfaces, likely formed during wafer fabrication, can be removed after annealing at 600°C for 1 h in air with a significant improvement of the RMS roughness to 0.126 nm and a terrace formation (Figure 6d). However, annealing at higher temperatures, above 800°C , makes the surface rougher that deteriorates with annealing temperature and

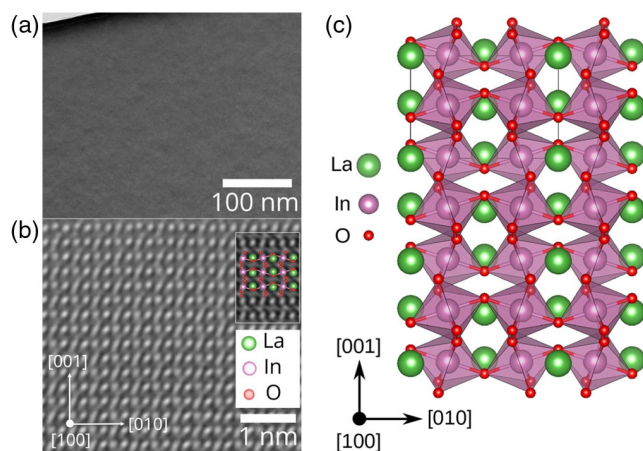


Figure 8. a) TEM bright field and b) HRTEM images of a melt-grown LaInO_3 sample, both viewed along the [100] crystallographic direction, and c) structural model of [100]-oriented LaInO_3 , where green, purple, and red balls correspond to La, In, and O atoms, respectively.

annealing time. This is the result of a slow surface decomposition at high temperatures, leading to In out-diffusion. Ba- and Ce-doped LaInO_3 wafers revealed a better surface stability at high temperatures as compared with undoped wafers.

SEM analysis of the wafers was conducted for as-grown (Figure 7a,b) and annealed wafers (Figure 7c,d). As-grown (001)- and (010)-oriented wafers are clear with no structural features. After annealing at 600°C for 1 h in air the wafer remained feature-less (Figure 7c), whereas after annealing at 1200°C , the surface was covered with islands (Figure 7d), which are In deficient according to an energy-dispersive X-ray analysis (not shown here).

To get the insight into the atomic structure of LaInO_3 (Figure 8c), a TEM analysis along the [100] crystallographic direction was conducted (Figure 8a,b). Figure 8a shows a typical TEM bright-field image. No dislocations or other extended defects are present. This holds for larger samples areas as well (not shown here). The high-resolution transmission electron microscopy (HRTEM) image shown in Figure 8b reveals a regular and defect-free pattern of the LaInO_3 crystal lattice. A HRTEM simulation overlaid with a ball-and-stick model of LaInO_3 is highlighted by a white frame and shown as an inset in Figure 8b. For the given focus (+11 nm) and sample thickness (4.08 nm), the simulation agrees excellently with the atomic pattern of LaInO_3 crystal. Under these conditions, the La atomic columns are represented as regular bright spots, and the In columns (surrounded by O atoms) are visible as smeared bright spots between the regular bright La columns.

2.3. Thermal Stability

For thermal stability check, LaInO_3 crystals samples were annealed in both oxidizing and reducing conditions: 1) in air up to 1300°C for 10 h and 2) in 5% $\text{H}_2 + \text{Ar}$ up to 800°C for 10 h. The crystal samples annealed in air (1) did not show any color or measurable mass change, but the surface deteriorated, as shown in Figure 7d. However, samples annealed in the presence of hydrogen exhibited color change already after annealing

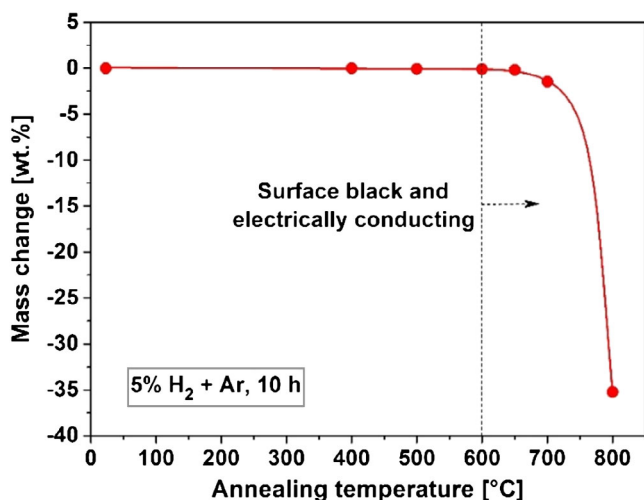


Figure 9. Temperature-dependent mass change of bulk LaInO_3 single crystals after annealing in reducing conditions (5% H_2 + Ar) for 10 h.

at 400 °C; they became a bit darker. As shown in **Figure 9**, annealing at 600–800 °C produced a mass loss from -0.1 wt% at 600 °C to -35 wt% at 800 °C and was accompanied by the formation of black surfaces of high electrical conductivity. Therefore, when using LaInO_3 crystals in reducing conditions for prolonged time, maximum temperature should not exceed about 400 °C to avoid crystal degradation. The mass loss is associated with the formation of gaseous In_2O and H_2O (oxygen from LaInO_3), the partial pressures of which (FactSage calculations) reach values of about 7×10^{-4} bar for In_2O and about 2×10^{-2} bar for H_2O at 800 °C.

Further insight into thermal stability of LaInO_3 single crystals provided thermal analysis comprising thermogravimetry (TG) (**Figure 10a**) and differential scanning calorimetry (DSC) (**Figure 10b, c**) measurements. The TG signals for two subsequent heating and cooling runs at 10 K min^{-1} in O_2 up to 1530 °C show a significant mass loss above 1300 °C. All curves reveal very similar slopes above 1300 °C, indicating the same thermal process pointing to the thermal decomposition and mass loss. A DSC curve of an as-grown sample (**Figure 10b**) reveals two exothermal effects at 1091 and 1424 °C that substantially disappear during the second heating run of the same sample. To further explore the thermal behavior of the crystallized compound, different heating/cooling rates of 3, 5, 10, 20 K min^{-1} were applied (**Figure 10c**), with a maximum temperature of 1180 °C to avoid thermal decomposition. Here, we can observe weakening of the first exothermal peak with next heating runs of the same sample and a shift toward higher temperatures with the heating rate. Again, during cooling (not shown), substantially no thermal effects were observed. Such a response is rather difficult to explain in terms of the second phase transition, as it is not reversible. Rather, thermally activated surface effects should be considered. Indeed, a polished wafer after similar thermal analysis (i.e., at heating rate of 10 K min^{-1} up to 1180 °C in O_2) showed surface deterioration.

To clarify the behavior of LaInO_3 crystals at high temperatures, a high-temperature XRD of a powdered crystal was conducted. **Figure 11a** shows XRD patterns taken at RT for 15 h

before heating the sample up, and next at 1000, 1200, 1300 °C for 3 h each, and at RT for 13 h after measurements. The analysis of the patterns did not reveal any new phases within the measurement accuracy, only relative change of some of the reflections and their tiny shift with temperature. In another study, the same sample was subjected to several cycles at 1200 °C for 3 h each (**Figure 11b**). After each of the cycles, the samples were cooled down to 500 °C and then heated up again to 1200 °C and held at that temperature for the predefined time. Also, in this case, we did not observe any phase transition or a creation of a new phase. A relative change of the intensity of some of the reflection with time (i.e., cycle) is here more pronounced. This study clearly shows that there is no phase transition in bulk LaInO_3 single crystals up to 1300 °C.

2.4. Optical Properties

Transmittance spectra of differently oriented wafers of 0.5 mm thickness prepared from as-grown LaInO_3 crystals (**Figure 12a**) revealed the absorption edges at about 400 nm. The crystals are transparent in both visible and near-infrared (NIR) spectral regions with no decrease in transmission with increasing wavelength. The transmittance spectra for all main wafer orientations well overlap with each other. Annealing wafers at temperatures above 1000 °C in the presence of oxygen leads to surface degradation (see **Figure 7**), which is clearly visible in the optical transmission spectra and strongly depends on the crystallographic orientation of the surface, as shown in **Figure 12b**. Repolishing annealed wafers restores the transmittance spectra to those before annealing (not shown).

A more detailed study of the absorption coefficients on much thinner samples (80 μm), as shown in **Figure 13**, clearly confirms the onset of fundamental absorption at about 4.3 eV (288 nm). As theory predicts a direct bandgap (see below), we extrapolated the corresponding direct optical bandgaps at RT for the three light polarizations of interest, which are 4.39 eV for the electric field vector $\mathbf{E} \parallel [100]$ and $[001]$ 4.35 eV for $\mathbf{E} \parallel [010]$.

Additional weak absorption (absorption coefficient of about 100 cm^{-1}) in the range between 2.8 and 4 eV is composed of at least two absorption bands peaking at about 3.15 and 3.8 eV. The variation of the corresponding peak intensities (10–20%) observed between different samples and sample positions without relation to the light polarization (not shown here) suggests that this absorption is related to defects/impurities.

A detailed investigation of the optical properties in the ideal LaInO_3 structure has been presented by some of the present authors^[26] using density functional theory (DFT) and many-body perturbation theory. Excellent agreement was found with the optical absorption measurements in terms of energy, intensity, and anisotropy. Importantly, the absorption edge at the optical gap of about 4.53 eV was found to be formed by very weak excitations. This characteristic of ideal LaInO_3 crystals was underpinned by ellipsometry measurements.^[25] The large calculated direct bandgap of 4.53 eV suggests that the experimentally observed weak absorption at 2.8–4 eV must be defect related. However, our experimental data do not indicate as to which type of defects is responsible for it, whether cation- or anion-related defects.

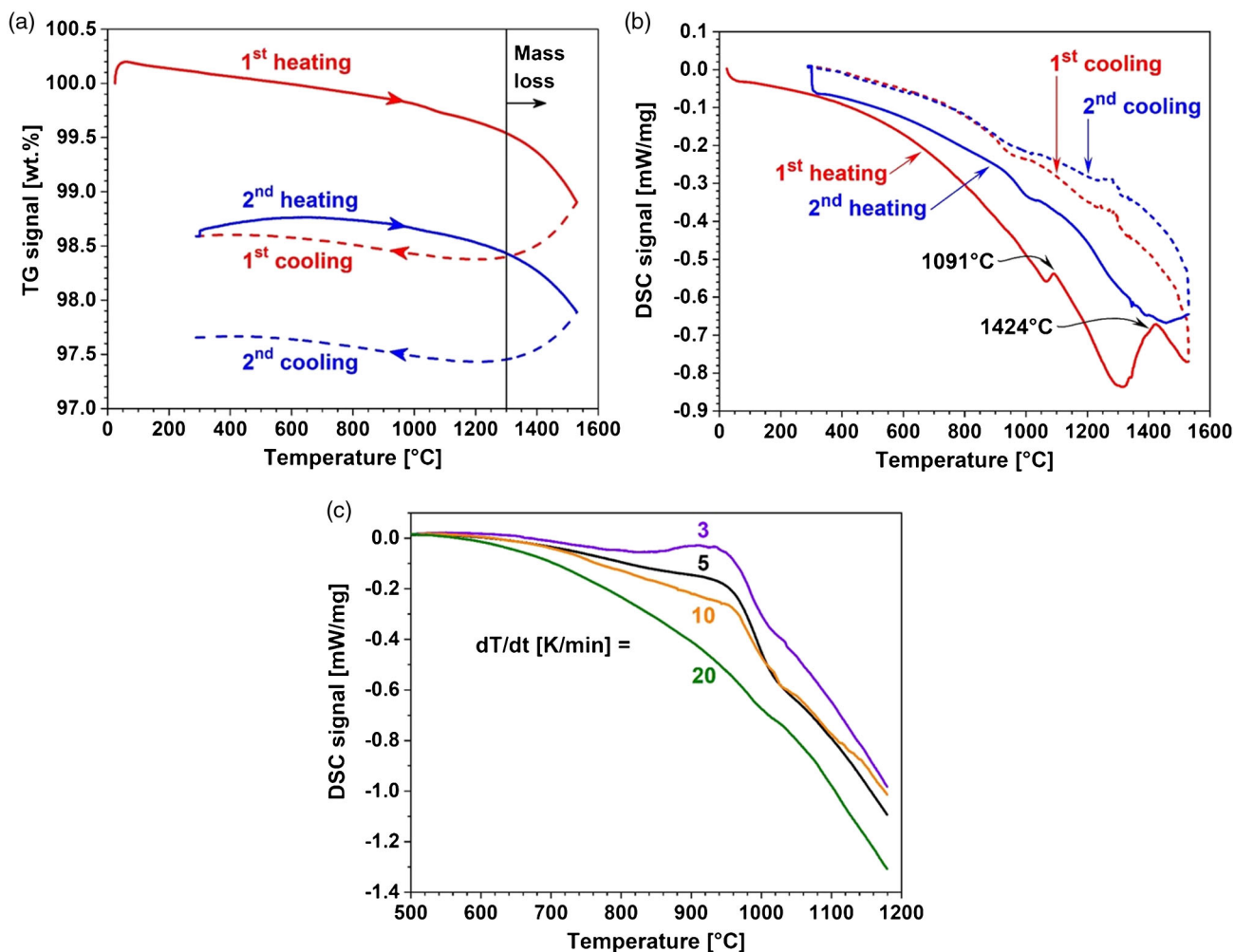


Figure 10. a) TG curves of two subsequent heating/cooling runs at a rate of 10 K min^{-1} , b) DSC curves of two subsequent heating/cooling runs at a rate of 10 K min^{-1} , and c) DSC curves of four subsequent heating runs at a rate of 3, 5, 10, and 20 K min^{-1} of a bulk LaInO_3 single crystal, always after intermediate cooling to 300°C .

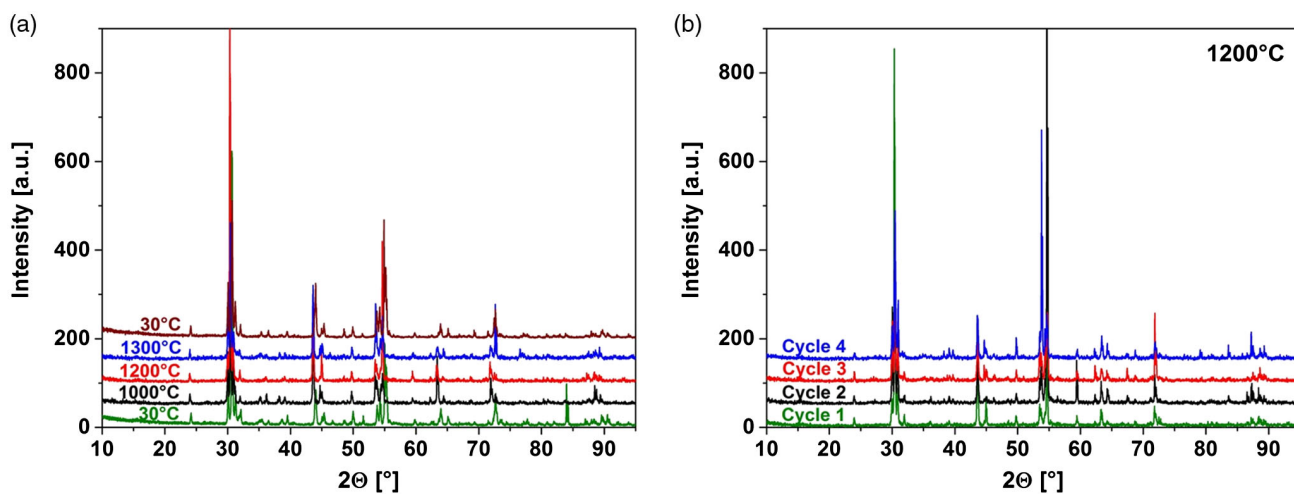


Figure 11. a) Temperature-dependent XRD patterns of a powdered crystal, up to 1300°C , and b) time-dependent XRD patterns of the powdered crystal at 1200°C .

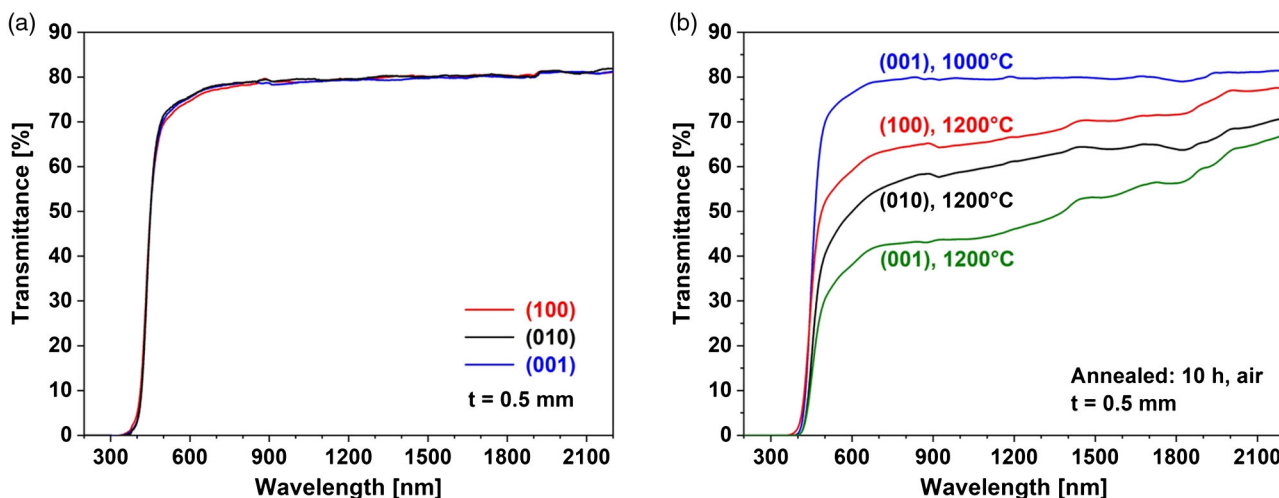


Figure 12. Transmittance spectra of a) as-grown and b) annealed LaInO_3 wafers of different orientations. The sample thickness was 0.5 mm in each case.

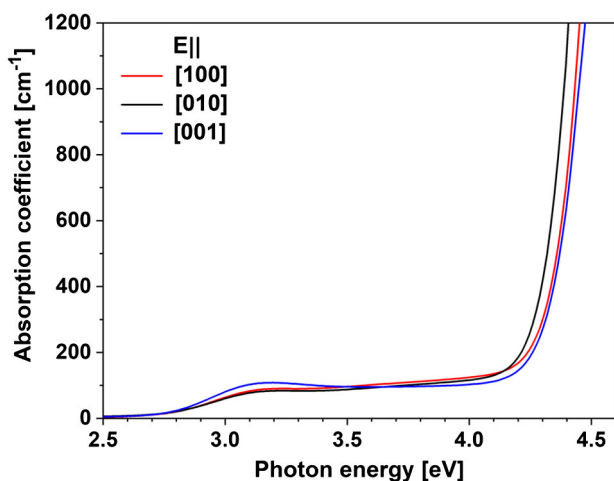


Figure 13. Absorption coefficient of melt-grown LaInO_3 wafers at RT for different polarizations of the \mathbf{E} vector of the light incident perpendicular to the wafer surface (001) (red and black lines) and (100) (blue line). Sample thickness was 80 μm .

To address this question, we computed band structures of defected LaInO_3 . The choice of $\delta = 0.0625$, corresponding to $\approx 6\%$, is motivated by our chemical analysis conducted for the cations La and In (Figure 4), which indicates that the crystals are very close to stoichiometric composition with a small deficiency of In ($\leq 6\%$). The calculated lattice constants of the orthorhombic LaInO_3 unit cell (Figure 14a) of $a = 5.939 \text{ \AA}$, $b = 8.210 \text{ \AA}$, and $c = 5.698 \text{ \AA}$ are in excellent agreement with the experimental values (see Section 3.2). As shown in Figure 14, we find that removal of the cations La or In, that act as acceptors, depletes the valence-band edge (red areas in Figure 14d,e), but the band structure of the pristine material (panel a) is largely preserved. An occupied midgap state appears in case of an oxygen vacancy that acts as an electron donor (Figure 14b,c). This feature is independent of whether the O atom is removed from LaO (termed O^{La}) or InO_2 (termed O^{In})

plane. Comparing the formation energies of the different supercells, we find that the structure with the oxygen vacancy O^{In} is most likely to form ($-2.55 \text{ eV atom}^{-1}$) followed by O^{La} ($-2.54 \text{ eV atom}^{-1}$), In ($-2.50 \text{ eV atom}^{-1}$), and La ($-2.44 \text{ eV atom}^{-1}$). Based on these results, we assign the weak absorption between 2.8 and 4 eV to oxygen vacancies. The chemical analysis of La and In concentrations, shown in Figure 4, revealing $\leq 6\%$ In deficiency, is in agreement with our finding that an In vacancy is energetically more favorable than a La vacancy.

Figure 15 shows cathodoluminescence (CL) spectra of differently oriented as-grown LaInO_3 wafers at RT. They all show a broad emission band roughly between 400 and 800 nm that peaks at 568 nm (2.18 eV) for all samples; therefore, it can be called a green emission. Such broad emission might be related to defects and/or self-trapped excitons. The absolute emission intensity is orientation dependent, the highest for as-grown (001)-oriented and the lowest for as-grown (010)-oriented samples. Whether this surface orientation dependence is due to different light extractions caused by distinct polarization of the excited luminescence or is due to surface preparation artifacts is still to be clarified. A CL spectrum of an annealed (001)-oriented sample (1000 $^\circ\text{C}$, 10 h, air) overlaps with the CL spectrum of the as-grown (001) sample. Moreover, at about 280 nm (4.4 eV), there is a feature that might correspond to a band-to-band transition, but it needs further investigation.

2.5. Electrical Properties

All as-grown LaInO_3 single crystals, whether undoped or doped with Ce or Ba, were electrically insulating. Annealing in the presence of oxygen for 10 h at 600–1300 $^\circ\text{C}$ did not induce any electrical conductivity, including the sample doped with Ba. Ba^{2+} ions substituting La^{3+} in the crystal lattice could induce the p-type conductivity, as reported in the literature for ceramic samples.^[27] However, in the case of melt-grown LaInO_3 single crystals, this did not happen even after annealing in the presence

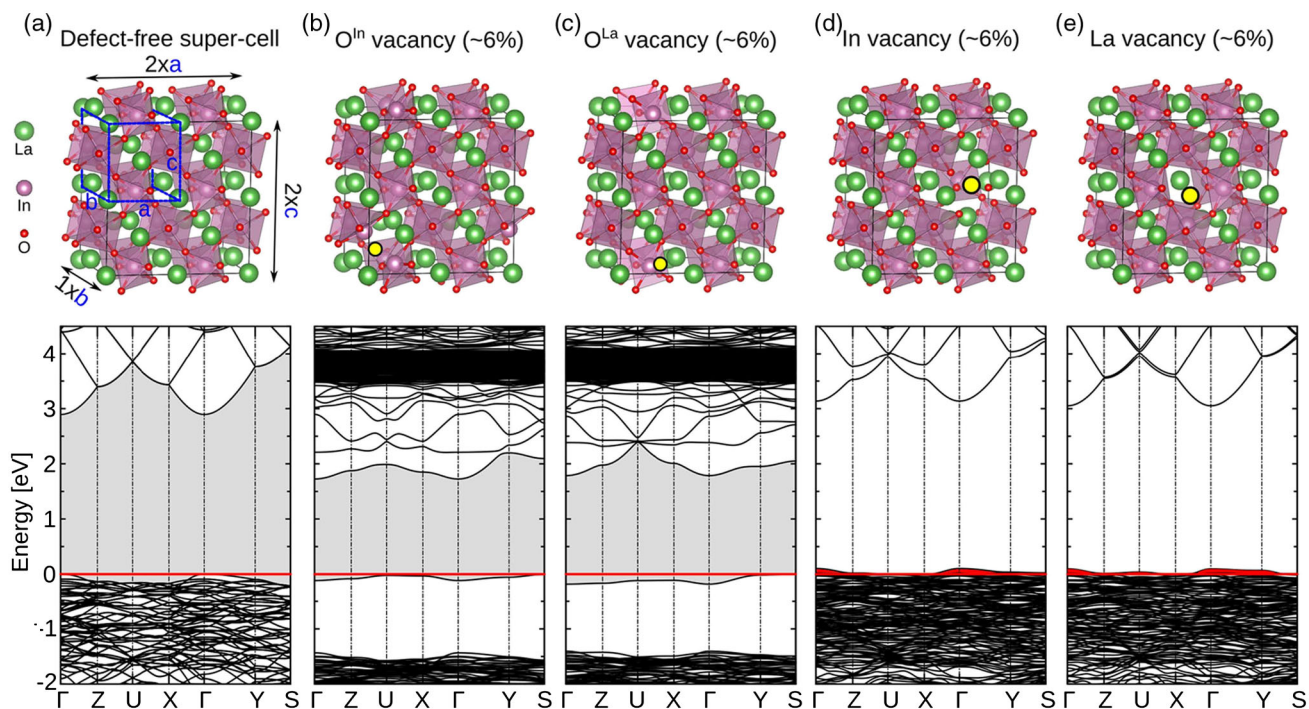


Figure 14. Top panels: $2 \times 1 \times 2$ supercells of LaInO_3 a) without defects (single unit cell indicated by blue lines) and with 6% deficiencies of b) O^{In} , c) O^{La} , d) In, and e) La. The defect positions are indicated by yellow spots. Bottom panels: the corresponding Kohn–Sham band structures. In the insulating structures (a, b, and c), the valence band edge is set to zero, and the bandgap is highlighted by a gray area. In the metallic structures (d,e), the Fermi level is set to zero, and the valence-band region that is depleted due to cation vacancies is highlighted by the red area. For a discussion on the quasiparticle bandgap of the pristine material, see the study by Park et al.^[25]

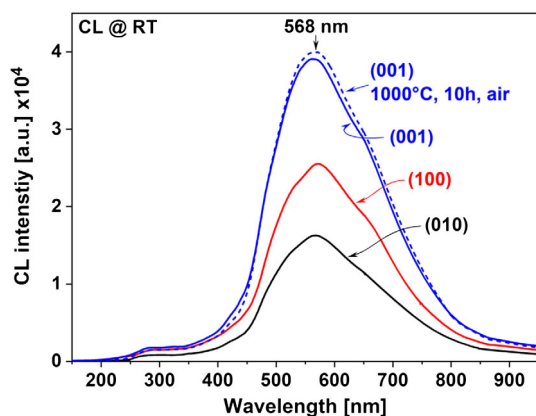


Figure 15. CL spectra at RT of differently oriented as-grown LaInO_3 wafers, including an annealed (001)-oriented sample.

of oxygen. Such annealing removes hydrogen that would potentially passivate Ba acceptors.

In contrast, annealing as-grown crystals in the presence of hydrogen at or above 600°C for 10 h made the crystal surface black and electrically conducting. Removing the surface layer by chemical etching in H_3PO_4 revealed the bulk crystals as yellowish and electrically insulating.

AC capacitance measurements of a plate capacitor structure containing an electrically insulating LaInO_3 wafer of (001)

surface orientation yielded a capacitance of 8.55 ± 0.05 pF. From this value, using the relation $C = \epsilon_r \epsilon_0 A/d$ (where ϵ_r is the relative static dielectric constant, ϵ_0 is the vacuum permittivity, A a surface area of the capacitor plate, and d the thickness of the LaInO_3 wafer), we calculated the relative static dielectric constant $\epsilon_r = 24.6 \pm 1.1$ along the [001] direction of LaInO_3 , which is comparable with $\epsilon_r = 23.7$ reported for bulk crystals obtained by the OFZ method.^[18] The values for bulk crystals differ, however, from 38.7 reported for heteroepitaxial LaInO_3 films^[5] and from a computed value of 32.^[22] Due to the high structural perfection of our crystals and the simple, macroscopic test structure used here, which mostly excludes artifacts such as interface charges that might be present in thin-film structures, we believe that the ϵ_r value given here ($\epsilon_{r,[001]} = 24.6 \pm 1.1$) represents a reliable intrinsic material parameter.

3. Conclusion

We obtained large bulk LaInO_3 single crystals directly from the melt with the use of the VGF method and Ir crucibles. LaInO_3 has a high MP of about 1880°C . It undergoes an incongruent decomposition and evaporation dominated by oxygen and In-containing species. Nonstoichiometric starting composition, high oxygen concentration in the growth atmosphere, and short growth time window produced large single crystals, enabling wafer fabrication with a large surface area ($10 \times 10 \text{ mm}^2$) of different orientations, high structural quality, and RMS roughness

down to 0.126 nm that makes the wafers suitable for epitaxy. The crystals are substantially stable up to about 800 and 400 °C upon annealing in the presence of oxygen and hydrogen, respectively, with no indication of any phase transition up to 1300 °C, above which a noticeable thermal decomposition takes place.

The experimental optical bandgap of 4.35–4.39 eV for direct transitions is polarization-dependent. Weak absorption between 2.8 and 4 eV is related to oxygen vacancies according to DFT calculations. CL spectra are dominated by a broad emission band peaking at 568 nm and consist of several contributions probably due to defects and/or self-trapped excitons. The relative static dielectric constant of a bulk LaInO₃ crystal is 24.6 ± 1.1 along the [001] crystallographic direction (*Pnma*).

All the as-grown LaInO₃ single crystals were electrical insulators, whether undoped or intentionally doped with Ba²⁺ or Ce³⁺, or annealed in the presence of oxygen. However, annealing in the presence of hydrogen made the crystal surface electrically conducting.

4. Experimental Section

Bulk Crystal Growth: Bulk LaInO₃ single crystals were grown by the VGF method in 40 mm-diameter iridium crucibles that were heated inductively. The growth atmosphere consisted of 9–14 vol.% O₂ and Ar at atmospheric pressure. Both heating-up and cooling-down times were between 5 and 8 h. As the starting material, La₂O₃ and In₂O₃ powders (4 N) were used, which were separately dried, mixed together, pressed, and sintered prior use. From the crystallized material, single-crystal grains with a volume of 0.5–2.5 cm³ were extracted and wafers of size up to 10 × 10 mm² were prepared.

Chemical Analysis: The main constituent and dopant concentrations were measured by an inductively coupled plasma–optical emission spectrometer (ICP–OES) equipment from Thermo Fisher Scientific GmbH (model iCAP 7400 DuoVoll MFC). The spectrometer was calibrated with synthetic solution standards. The samples were prepared by microwave digestion with 5 ml HNO₃ + 1 ml H₂O₂ at 200 °C for 20 min.

X-Ray Characterization: The crystal structure was evaluated using several techniques: 1) X-ray powder diffraction (XRD) of a powdered crystal using a diffractometer utilizing a Bragg–Brentano design with a Cu-K- α 1/2 radiation source. The same equipment was applied for lattice constant determination using Si powder as an external standard. 2) For temperature-dependent XRD measurements, a furnace from Mri GmbH (Karlsruhe) in the version TC-Basic (TC-m-05-06) with a PtRh-direct heater-type S was utilized. The measurements were carried out in air. 3) Rocking curves were measured using a high-resolution X-ray diffractometer system (HR XRD) Master (Seifert) equipped with a Bartels monochromator Ge (220) and by choosing an aperture of 0.2 mm.

Optical Transmittance: The spectra were recorded at RT using a spectrophotometer Lambda 19 (PerkinElmer) in the wavelength range from 200 to 2200 nm. To minimize scattering losses, an integrating sphere was used. The crystal samples were double side polished to a thickness of 0.5 mm. For the measurement of the near-edge absorption spectra, thin samples of 80 μ m, an aperture of 4 mm diameter, and reference beam attenuation to 1% were used.

Transmission Electron Microscopy (TEM): The analysis was conducted with a spherical aberration-corrected FEI Titan 80-300 microscope operating at 300 kV, with the corrector set to a Cs = –15 μ m. Plane-view TEM samples were prepared by tripod polishing followed by argon ion milling at liquid nitrogen temperature using Precision Ion Polishing System (PIPS) at beam energies of 3.5–0.2 keV.

Scanning Electron Microscopy (SEM): Secondary electron contrast was used in a Nova 600 (FEI) microscope to image the surface topology of the crystal samples.

Atomic Force Microscopy (AFM): A “Dimension Icon” equipment from Bruker was used. Measurements were carried out in a “peak force tapping” mode with a scan rate of 0.5 lines per second and 384 points per line in the X- and Y-directions.

Cathodoluminescence (CL): CL spectra were taken with a Gatan Monarc system at RT with a voltage and current of 20 keV and 1.6 nA, respectively.

Relative-Static Dielectric Constant: Conducted by AC capacitance measurements of a plate capacitor structure consisting of an electrically insulating LaInO₃ wafer of size 7 × 7 × 0.5 mm³, and circular Au contacts of 5 mm in diameter and 50 nm in thickness on the opposite sides of the LaInO₃ wafer. The capacitance was measured using HP4284A precision LCR meter (Hewlett Packard) at zero bias between 1 kHz and 1 MHz.

Electrical Properties: The Hall effect of the crystals was measured in van der Pauw configuration at RT using a Hall measurement system HMS 7504 (Lake Shore). The contacts were prepared by rubbing an In–Ga eutectic mixture at four points on the rim of wafer-shaped samples of 5 × 5 × 0.5 mm³ in size. Electrical setup and sample dimensions limited resistivity measurements to values up to about 10⁸ Ω cm. Therefore, samples with higher resistivity could not be measured and are indicated as electrical insulators.

Thermal Analysis: DSC and simultaneous TG were conducted up to 1530 or 1180 °C in oxygen with the Netzsch-type STA 449 C and STA 409 CD equipment using the LaInO₃ single crystal as a sample and Pt crucibles acting as sample and reference crucibles, respectively.

Thermodynamic Calculations: Thermodynamic calculations were carried out using the FactSage software package^[28] to get information on the activity of the species relevant for melt growth of LaInO₃ single crystals.

DFT Calculations: The optimized crystal structure and the electronic properties were obtained using the generalized gradient approximation in the PBEsol parameterization^[19] for the exchange–correlation effects.^[29,30] All calculations were carried out using FHI-aims,^[31] an all-electron full-potential package using numerical atom-centered orbitals. For all atomic species, we used a “tight” setting with a “tier” 2 basis set for oxygen, “tier 1+hfdg” for lanthanum, and “tier 1+gpfhp” for indium. The convergence criteria were 10^{–6} electrons for the density, 10^{–6} eV for the total energy, 10^{–4} eV \AA^{-1} for the forces, and 10^{–4} eV for the eigenvalues. To simulate deficiencies $\delta = 0.0625$ atoms per LaInO₃ formula unit, we removed either one La, In, or O from an 80-atom 2 × 1 × 2 supercell, that is, La₁₅In₁₆O₄₈, La₁₆In₁₅O₄₈, and La₁₆In₁₆O₄₇. Lattice constants and internal coordinates were optimized for all systems until the residual force on each atom was less than 0.001 eV \AA^{-1} . Brillouin zone integrations were conducted on a 4 × 6 × 4 k-grid. Atomic structures were visualized using the software package VESTA.^[32] We computed the formation energy E_f for the three structures to rank their relative stability as $E_f = \frac{1}{N} [E_{\text{tot}}^{\text{vac}} - \sum_{\text{elements}} E_{\text{tot}}^{\text{bulk}}]$, where $E_{\text{tot}}^{\text{vac}}$ represents the total energy of the supercell with vacancy i ($i = \text{La, In, or O}$) and E_{free} that of defect-free supercell with a vacancy (vac = La, In, or O). $E_{\text{tot}}^{\text{bulk}}$ was the total energy per atom of the constituent elements in their corresponding stable bulk reference structure (fcc for La, face-centered tetragonal for In) or O₂ molecule. Division by number of atoms N (here $N = 79$) provided the formation energy in eV per atom.

Acknowledgements

The present work was supported by the Leibniz Senatsausschuss Wettbewerb (SAW) project BASTET and conducted in the framework of GraFOx, a Leibniz science campus partially funded by the Leibniz Association. The authors acknowledge the North-German Supercomputing Alliance (HLRN) for providing HPC resources that have contributed to the research results reported in this manuscript (project bep00078). The authors express their gratitude to Frank M. Kießling from the Leibniz-Institut für Kristallzüchtung for critical reading of the manuscript.

Open access funding enabled and organized by Projekt DEAL.

Conflict of Interest

The authors declare no conflict of interest.

Data Availability Statement

Input and output files related to Figure 14 can be downloaded free of charge from the NOMAD Repository^[33] at the following link: <https://dx.doi.org/10.17172/NOMAD/2021.03.16-1>.

Keywords

bandgaps, band structures, LaInO_3 , melt growth, single crystals, wafers

Received: January 11, 2021

Revised: April 12, 2021

Published online: July 17, 2021

-
- [1] H. P. He, X. J. Huang, L. Q. Chen, *Electrochim. Acta* **2001**, *46*, 2871.
- [2] H. P. He, X. J. Huang, L. Q. Chen, *Ionics* **2000**, *6*, 64.
- [3] H. P. He, X. J. Huang, L. Q. Chen, *Solid State Ion.* **2000**, *130*, 183.
- [4] X. Liu, J. Lin, *Solid State Sci.* **2009**, *11*, 2030.
- [5] U. Kim, C. Park, T. Ha, Y. M. Kim, N. Kim, C. Ju, J. Park, J. Yu, J. H. Kim, K. Char, *APL Mater.* **2015**, *3*, 036101.
- [6] U. Kim, C. Park, Y. M. Kim, J. Shin, K. Char, *APL Mater.* **2016**, *4*, 071102.
- [7] Y. Kim, Y. M. Kim, J. Shin, K. Char, *APL Mater.* **2018**, *6*, 096104.
- [8] W. Aggoune, C. Draxl; arXiv:2103.07216 (2021).
- [9] A. J. Smith, A. J. E. Welch, *Acta Crystallogr.* **1960**, *13*, 653.
- [10] X. Luo, Y. S. Oh, A. Sirenko, P. Gao, T. A. Tyson, K. Char, S.-W. Cheong, *Appl. Phys. Lett.* **2012**, *100*, 172112.
- [11] H. J. Kim, U. Kim, H. M. Kim, T. H. Kim, H. S. Mun, B.-G. Jeon, K. T. Hong, W.-J. Lee, C. Ju, K. H. Kim, K. Char, *Appl. Phys. Express* **2012**, *5*, 061102.
- [12] W.-J. Lee, H. J. Kim, J. Kang, D. H. Jang, T. H. Kim, J. H. Lee, K. H. Kim, *Annu. Rev. Mater. Res.* **2017**, *47*, 391.
- [13] T. N. Stanislavchuk, A. A. Sirenko, A. P. Litvinchuk, X. Luo, S.-W. Cheong, *J. Appl. Phys.* **2012**, *112*, 044108.
- [14] E. McCalla, D. Phelan, M. J. Krogstad, B. Dabrowski, C. Leighton, *Phys. Rev. Meter.* **2018**, *2*, 084601.
- [15] Z. Galazka, R. Uecker, K. Irmscher, D. Klimm, R. Bertram, A. Kwasniewski, M. Naumann, R. Schewski, M. Pietsch, U. Juda, A. Fiedler, M. Albrecht, S. Ganschow, T. Markurt, C. Gugushev, M. Bickermann, *J. Phys.: Condens. Matter.* **2017**, *29*, 075701.
- [16] S. K. Chaluvadi, V. Aswin, P. Kumar, P. Singh, D. Haranath, P. K. Rout, A. Dogra, *J. Lumin.* **2015**, *166*, 244.
- [17] C. Lau, Y. Kim, S. Albright, K. Char, C. H. Ahn, F. J. Walker, *APL Mater.* **2019**, *7*, 031108.
- [18] D. H. Jang, W.-J. Lee, E. Sohn, H. J. Kim, D. Seo, J.-Y. Park, E. J. Choi, K. H. Kim, *J. Appl. Phys.* **2017**, *121*, 125109.
- [19] Z. Galazka, R. Uecker, R. Fornari, *J. Cryst. Growth* **2014**, *388*, 61.
- [20] Z. Galazka, R. Uecker, K. Irmscher, D. Schulz, D. Klimm, M. Albrecht, M. Pietsch, S. Ganschow, A. Kwasniewski, R. Fornari, *J. Cryst. Growth* **2013**, *362*, 349.
- [21] Z. Galazka, S. Ganschow, R. Schewski, K. Irmscher, D. Klimm, A. Kwasniewski, M. Pietsch, A. Fiedler, I. Schulze-Jonack, M. Albrecht, T. Schröder, M. Bickermann, *APL Mater.* **2019**, *7*, 022512.
- [22] E. Ruiz-Trejo, G. Tavizón, A. Arroyo-Landeros, *J. Phys. Chem. Solids* **2003**, *64*, 515.
- [23] www.icdd.com.
- [24] R. S. Ruth, *J. Res. Natl. Bur. Stand.* **1957**, *58*, 2736.
- [25] H. M. Park, H. J. Lee, S. H. Park, H. I. Yoob, *Acta Cryst.* **2003**, *C59*, i131.
- [26] W. Aggoune, K. Irmscher, D. Nabok, C. Vona, S. Bin Anooz, Z. Galazka, M. Albrecht, C. Draxl, *Phys. Rev. B* **2021**, *103*, 115105.
- [27] H. L. Kim, K. H. Lee, S. Kim, H. L. Lee, *Jpn. J. Appl. Phys.* **2006**, *45*, 872.
- [28] www.factsage.com (accessed: September 2020), for FactSage 7.2002C, **2018**.
- [29] P. Hohenberg, W. Kohn, *Phys. Rev.* **1964**, *136*, B864.
- [30] W. Kohn, L. J. Sham, *Phys. Rev.* **1965**, *140*, A1133.
- [31] V. Blum, R. Gehrke, F. Hanke, P. Havu, V. Havu, X. Ren, K. Reuter, M. Scheffler, *Comput. Phys. Commun.* **2009**, *180*, 2175.
- [32] K. Momma, F. Izumi, *J. Appl. Cryst.* **2011**, *44*, 1272.
- [33] C. Draxl, M. Scheffler, *J. Phys. Mater.* **2019**, *2*, 036001.